Deformation of the lowermost mantle from seismic anisotropy

Andy Nowacki, James Wookey & J-Michael Kendall

Department of Earth Sciences, University of Bristol, Wills Memorial Building, Queen's Road, Bristol, BS8 1RJ, UK

Understanding the lowermost part of the Earth's mantle—known as D″—can help us investigate whole-mantle dynamics, core-mantle interactions and processes such as slab deformation in the deep Earth. D″ shows significant seismic anisotropy, the variation of seismic wave speed with direction[1–5]. This is likely due to deformation-induced alignment of $MgSiO_3$-post-perovskite (ppv), believed to be the main mineral phase present in the region; however if this is the case, then previous measurements of D″ anisotropy, which are generally made in one direction only, are insufficient to distinguish candidate mechanisms of slip in ppv because the mineral is orthorhombic. Here we measure anisotropy in D″ beneath North and Central America, where slab material impinges[6] on the core-mantle boundary (CMB), using shallow as well as deep earthquakes to increase the azimuthal coverage in D″. We make >700 individual measurements of shear wave splitting in D″ in three regions from two different azimuths in each case, and we show that the previously-assumed[2,3,7] case of vertical transverse isotropy (VTI, where wave speed shows no azimuthal variation) is not possible; more complicated mechanisms must be involved. We test the fit of different $MgSiO_3$-ppv deformation mechanisms to our results and find that shear on (001) is most consistent with observations and expected shear above the CMB beneath subduction zones. With new models of mantle flow, or improved experimental evidence of which ppv slip systems dominate, this method will allow us to map deformation at the CMB and link processes in D″, such as plume initiation, to the rest of the mantle.

Studies of D″ anisotropy in the Caribbean are numerous[2–4,7–9], because of an abundance of deep earthquakes in South America and seismometers in North America, and show ~1% shear wave anisotropy. These mostly compare the horizontally- (SH) and vertically-polarised (SV) shear waves, assuming a style of anisotropy where the shear wave velocity V_S varies only with the angle away from the vertical (vertical transverse isotropy, VTI). With this assumption, SH leads SV here, corresponding to $\varphi'=\pm 90^\circ$ in our notation (Fig. 1c). A further limitation is using only one azimuth of rays in D″: this cannot distinguish VTI from the case of an arbitrarily tilted axis of rotational symmetry in which wave speed does not vary (tilted transverse isotropy, TTI) when the axis dips towards the receivers or stations. An improvement on this situation can be made by utilising crossing ray paths in D″ [10], but this relies on having the correct source-receiver geometry, which is not possible beneath North America using only deep earthquakes. We address this issue beneath the Caribbean by incorporating measurements from shallow earthquakes in our dataset, and thus reduce the symmetry of the anisotropy which must be assumed.

We measure anisotropy in D″ using differential splitting in S and ScS phases using an approach described by refs. [10,11]. Both phases travel through the same region of the upper mantle (UM), but only ScS samples D″ (Fig. 1a). As the majority of the lower mantle (LM) is relatively isotropic[12], by removing the splitting introduced in the UM we can measure that which occurs only in D″ (see Supplementary Information). Earthquakes in South and Central America, Hawaii, the East Pacific Rise (EPR) and the Mid-Atlantic Ridge (MAR), detected at North American stations, provide a dense coverage of crossing rays which traverse D″ beneath southern North America and the Caribbean (Fig. 1b). Three distinct regions are covered (Fig. 2), each sampled along two distinct azimuths. The Caribbean (region ‘S’) has been previously well studied[1,4,8], but the northeast (‘E’) and southwest (‘W’) United States have not.

Stacked results along each azimuth in the three regions give splitting parameters shown in Figure 2 and listed in Supplementary Table 3. We discuss results in terms of the delay time (δt) and ray frame fast orientation (φ'; Figure 1c). The primary observation is that D″ everywhere shows anisotropy of between 0.8% and 1.5% (assuming a uniform 250 km-thick D″ layer). Along south–north (region 'S') and southeast–northwest ('E') ray paths, from deep South American events (~200 measurements), δt=(1.45±0.55) s, implying shear wave anisotropy of ~0.8%. Fast orientations are approximately CMB-parallel ($\varphi' \approx 90^\circ$). This agrees with previous studies made along similar azimuths[4,7–9], including the presence of some small variation in φ' of up to $\pm 15^\circ$ [4,8]. Such variations could be approximated as VTI over the region. Detailed results are shown in Supplementary Figs. 1 and 11. Notably, however, oblique to the ~south–north raypaths in the Caribbean, fast directions are at least 40° from CMB-parallel (region S: δt=1.68 s, $\varphi'=-42^\circ$; region E: δt=1.28 s, $\varphi'=45^\circ$). In region 'W', both azimuths show φ' about 10–15° from the horizontal in D″, with δt~1.2 s. Hence nowhere are our measurements compatible with VTI, because we do not find $\varphi' = \pm 90^\circ$ within error in both directions for any region.

A likely mechanism for the production of anisotropy in D″ is the lattice-preferred orientation (LPO) of anisotropic mineral phases present above the CMB such as (Mg,Fe)O, and $MgSiO_3$-perovskite (pv) and -postperovskite (ppv). These may give rise to styles of anisotropy more complicated than TTI with lower symmetries, which are compatible with our two-azimuth measurements. We investigate the possibility of LPO in ppv leading to the observed anisotropy rather than other phases because of its likely abundance in seismically fast regions of the lowermost mantle (LMM) beneath North America and its relatively large anisotropy. (Mg,Fe)O and pv seem poor candidates for D″ anisotropy—(Mg,Fe)O is equally abundant in the LM above D″, which appears relatively isotropic[12], and pv is the dominant phase there. Whilst (Mg,Fe)O may be strongly anisotropic and mechanically weaker than ppv[13–15], and therefore might take up

more deformation and align more fully, ppv is also highly anisotropic and is the most abundant phase, meaning a lower degree of alignment of ppv can produce just as much anisotropy as more alignment of (Mg,Fe)O. Therefore LPO in ppv is our preferred mineralogical mechanism.

Different candidate mechanisms for LPO development in ppv from deformation by dislocation creep have been proposed: slip systems of $[\bar{1}\ 10](110)$[16–18] and [100](010)[19–21] have been inferred from experimental and theoretical methods. Recent experimental work[22] has also suggested that the [100](001) system may be plausible, which is appealing since it appears to best match the first-order anisotropic signature of the lowermost mantle[23–26].

Our results can differentiate between these candidate mechanisms if we assume that most of the measured anisotropy in D″ is a result of deformation-induced LPO in ppv, and we have an accurate estimate of the mantle flow where we measure anisotropy. At present, such models of mantle deformation are in their infancy, but we can nonetheless make inferences from broad-scale trends in subduction and global V_S models. We calculate the orientations of the shear planes and slip directions which are compatible with our measurements for the three slip systems in ppv. Aggregate elastic constants for the $[\bar{1}\ 10]$ (110) and [001](010) systems are taken from deformation experiments[17,20]; we use single-crystal elastic constants from first-principles calculations[23,25] for the [100](001) system. These planes and directions are plotted in Fig. 3. We also produce the shear planes predicted for cases of pv and MgO (Supplementary Fig. 11).

At present, there is some disagreement in detail between different *ab initio* elastic constants for ppv[23,27]. We use those of ref. [23] for consistency with experimental studies.

Another source of uncertainty may be the extrapolation of results of deformation experiments[16,17,20,22] to LMM conditions.

To guide our interpretation of the results, we can appeal to the broadly analogous situation of finite strain and olivine LPO associated with passive upwelling beneath a mid-ocean ridge. Models indicate that, near the centre of the upwelling, directions of maximum finite extension dip away from the centre, and become more horizontal with distance from the ridge[28]. Corresponding features beneath downwellings are found in convection models of the lower mantle—inclined deformation dipping towards the downwelling centre[29]. Regions E and S are either side of the apparent centre of the downwelling Farallon slab[6,30] (Figs. 2, 3) which strikes roughly northwest-southeast, hence we postulate northeast-southwest slip directions on inclined shear planes with an opposite sense of dip (*i.e.*, dipping southwest for region E, northeast for region S). Further away from the downwelling, in region W, more horizontal flow is expected and hence a horizontal shear plane with northeast-southwest slip directions.

All three considered slip systems have orientations which can explain the data, however the predictions of the [100](001) slip system (Fig. 3) best match the above criteria. The [$\bar{1}$ 10] (110) system is arguably the least plausible, as it requires complex flow further from the downwelling (region W) where a simpler horizontal flow pattern is expected. We cannot yet completely rule out the [100](010) system; more rigorous flow modelling in the region is required to conclusively resolve this issue.

The slip systems predicted for pv and MgO (Supplementary Fig. 12) seem less likely, particularly where the measured splitting is high. The presence of pv versus ppv in D″ in region S, for instance, cannot account for the high anisotropy inferred, and shear planes and directions for MgO are mostly very steep.

D″ anisotropy might also arise from shape-preferred orientation (SPO) of seismically distinct material over sub-wavelength scales. This would lead to a TTI-type behaviour[2], with which our observations are compatible. In this case, we can interpret our results simply by finding the common plane, normal to the rotational symmetry axis, from the two azimuths and φ'. These planes are shown in Supplementary Fig. 2.

In each region, the TTI plane dips approximately in the same way as for the [100](010) case, i.e. southwest, southeast and south in regions W, S and E respectively, by between 26–52° (Supplementary Fig. 2). However, there is no constraint on the slip direction, and especially in regions S and E, where the dip is $\sim 50^\circ$, it is hard to correlate the TI planes with a candidate plane of deformation based on V_S, and models of deformation suggest strain in such slab-parallel orientations is unlikely. For this reason and other explanations of D″ properties by the post-perovskite phase[25], we favour the mineralogical interpretation at present, where all tested ppv mechanisms are in some agreement with our results, and the [100](001) slip system in ppv is most compatible with our observations.

We have made significant progress towards using D″ anisotropy to measure deformation in the LMM. Assuming that anisotropy in D″ is caused by the alignment of ppv, we may suggest which slip system dominates LPO, though without more detailed models of mantle flow there is still doubt as to the likely orientation of slip planes and directions in the LMM. As more reliable estimates of the type of deformation we expect in well-studied regions become available, or conversely as numerical and physical experiments further indicate the mechanisms by which the material in D″ deforms, our observations of seismic anisotropy hold great potential to map dynamic processes at the CMB.

Methods Summary

We measured differential shear wave splitting between S and ScS recorded at ~500 seismic stations in North and Central America, using events of $M_W \geq 5.7$, epicentral distance 55–82° (Supplementary Table 3). Data were bandpass filtered between 0.001–0.3 Hz to remove noise. We analysed splitting in the phases using the minimum eigenvalue technique (Supplementary Fig. 3). We correct for upper mantle (UM) anisotropy using published[31,32] SKS splitting measurements at stations showing little variation of parameters with backazimuth—corresponding to simple UM anisotropy—where there are measurements along similar backazimuths to S–ScS used here. Measuring splitting in S with a receiver-side correction gives an estimate of the source-side splitting beneath the earthquake (Fig. 1b; Supplementary Table 3). Both corrections are applied when analysing ScS: the measurement is thus of splitting in D″ alone.

We confirm that the only source of splitting in our measurements is D″ by comparing: (1) splitting in S from a deep event with that in SKS; (2) the source-side anisotropy with SKS measurements at the source; (3) the initial polarisation of S after analysis with that predicted by the GlobalCMT solution; (4) the consistency of measurements when correcting with real SKS and randomised receiver corrections; (5) φ' and δt along the same ray paths for deep and shallow events, correcting the latter for UM anisotropy. (See online methods and Supplementary Figs. 5–9 for details.)

Orientations of shear planes and slip directions in each slip system of ppv are computed by grid search over the elastic constants[16,20,25], which are rotated about the three principal axes. Shear wave splitting is calculated, and orientations which are compatible with the observations are plotted. The constants are scaled linearly away from the isotropic case to fit the observations, and this scaling is shown by colour (Fig. 3b–j), qualitatively representing strain.

Received 21 January 2010; accepted 25 August 2010.

1. Kendall, J.-M. & Silver, P. Constraints from seismic anisotropy on the nature of the lowermost mantle. *Nature* **381**, 409–412 (1996).

2. Kendall, J.-M. & Silver, P. G. Investigating causes of D″ anisotropy. In Gurnis, M., Wysession, M. E., Knittle, E. & Buffett, B. A. (eds.) *The Core–Mantle Boundary Region*, 97–118 (American Geophysical Union, Washington, D.C., 1998).

3. Lay, T., Williams, Q., Garnero, E. J., Kellogg, L. & Wysession, M. E. Seismic wave anisotropy in the D″ region and its implications. In Karato, S., Stixrude, L., Liebermann, R. C., Masters, G. & Forte, A. (eds.) *The Core–Mantle Boundary Region*, 299–318 (American Geophysical Union, Washington, D.C., 1998).

4. Maupin, V., Garnero, E. J., Lay, T. & Fouch, M. J. Azimuthal anisotropy in the D″ layer beneath the Caribbean. *J Geophys Res-Sol Ea* **110**, B08301 (2005).

5. Long, M. D. Complex anisotropy in D″ beneath the eastern pacific from SKS–SKKS splitting discrepancies. *Earth Planet Sci Lett* **283**, 181–189 (2009).

6. Ren, Y., Stutzman, E., van der Hilst, R. D. & Besse, J. Understanding seismic heterogeneities in the lower mantle beneath the Americas from seismic tomography and plate tectonic history. *J Geophys Res-Sol Ea* **112**, B01302 (2007).

7. Kendall, J.-M. & Nangini, C. Lateral variations in D″ below the Caribbean. *Geophys Res Lett* **23**, 399–402 (1996).

8. Garnero, E. J., Maupin, V., Lay, T. & Fouch, M. J. Variable azimuthal anisotropy in Earth's lowermost mantle. *Science* **306**, 259–261 (2004).

9. Rokosky, J. M., Lay, T. & Garnero, E. J. Small-scale lateral variations in azimuthally anisotropic D″ structure beneath the Cocos plate. *Earth Planet Sci Lett* **248**, 411–425 (2006).

10. Wookey, J. & Kendall, J.-M. Constraints on lowermost mantle mineralogy and fabric beneath Siberia from seismic anisotropy. *Earth Planet Sci Lett* **275**, 32–42 (2008).

11. Wookey, J., Kendall, J.-M. & Rumpker, G. Lowermost mantle anisotropy beneath the north Pacific from differential S–ScS splitting. *Geophys J Int* **161**, 829–838 (2005).

12. Meade, C., Silver, P. & Kaneshima, S. Laboratory and seismological observations of lower mantle isotropy. *Geophys Res Lett* **22**, 1293–1296 (1995).

13. Karki, B., Wentzcovitch, R., de Gironcoli, S. & Baroni, S. First-principles determination of elastic anisotropy and wave velocities of MgO at lower mantle conditions. *Science* **286**, 1705–1707 (1999).

14. Long, M. D., Xiao, X., Jiang, Z., Evans, B. & Karato, S. Lattice preferred orientation in deformed polycrystalline (Mg,Fe)O and implications for seismic anisotropy in D″. *Phys. Earth Planet. Inter.* **156**, 75–88 (2006).

15. Yamazaki, D. & Karato, S. Fabric development in (Mg,Fe)O during large strain, shear deformation: implications for seismic anisotropy in Earth's lower mantle. *Phys. Earth Planet. Inter.* **131**, 251–267 (2002).

16. Merkel, S. *et al.* Deformation of (Mg,Fe)SiO_3 post-perovskite and D″ anisotropy. *Science* **316**, 1729–1732 (2007).

17. Merkel, S. *et al.* Plastic deformation of $MgGeO_3$ post-perovskite at lower mantle pressures. *Science* **311**, 644–646 (2006).

18. Oganov, A., Martonak, R., Laio, A., Raiteri, P. & Parrinello, M. Anisotropy of Earth's D″ layer and stacking faults in the $MgSiO_3$ post-perovskite phase. *Nature* **438**, 1142–1144 (2005).

19. Carrez, P., Ferré, D. & Cordier, P. Implications for plastic flow in the deep mantle from modelling dislocations in $MgSiO_3$ minerals. *Nature* **446**, 68–70 (2007).

20. Yamazaki, D., Yoshino, T., Ohfuji, H., Ando, J. & Yoneda, A. Origin of seismic anisotropy in the D″ layer inferred from shear deformation experiments on post-perovskite phase. *Earth Planet Sci Lett* **252**, 372–378 (2006).

21. Iitaka, T., Hirose, K., Kawamura, K. & Murakami, M. The elasticity of the $MgSiO_3$ post-perovskite phase in the Earth's lowermost mantle. *Nature* **430**, 442–445 (2004).

22. Okada, T., Yagi, T., Niwa, K. & Kikegawa, T. Lattice-preferred orientations in post-perovskite-type $MgGeO_3$ formed by transformations from different pre-phases. *Phys. Earth Planet. Inter.* **180**, 195–202 (2010).

23. Stackhouse, S., Brodholt, J. P., Wookey, J., Kendall, J.-M. & Price, G. D. The effect of temperature on the seismic anisotropy of the perovskite and post-perovskite polymorphs of $MgSiO_3$. *Earth Planet Sci Lett* **230**, 1–10 (2005).

24. Tsuchiya, T., Tsuchiya, J., Umemoto, K. & Wentzcovitch, R. Phase transition in $MgSiO_3$ perovskite in the Earth's lower mantle. *Earth Planet Sci Lett* **224**, 241–248 (2004).

25. Wookey, J., Stackhouse, S., Kendall, J.-M., Brodholt, J. P. & Price, G. D. Efficacy of the post-perovskite phase as an explanation for lowermost-mantle seismic properties. *Nature* **438**, 1004–1007 (2005).

26. Wookey, J. & Kendall, J.-M. Seismic anisotropy of post-perovskite and the lowermost mantle. In Hirose, K., Brodholt, J., Lay, T. & Yuen, D. (eds.) *Post-Perovksite: The Last Mantle Phase Transition*, 171–189 (American Geophysical Union, Washington, D.C., 2007).

27. Wentzcovitch, R., Tsuchiya, T. & Tsuchiya, J. $MgSiO_3$ postperovskite at D″ conditions. *P Natl Acad Sci Usa* **103**, 543–546 (2006).

28. Blackman, D. *et al.* Teleseismic imaging of subaxial flow at mid-ocean ridges: Traveltime effects of anisotropic mineral texture in the mantle. *Geophys J Int* **127**, 415–426 (1996).

29. McNamara, A., van Keken, P. & Karato, S. Development of finite strain in the convecting lower mantle and its implications for seismic anisotropy. *J Geophys Res-Sol Ea* **108**, 2230 (2003).

30. Ritsema, J., van Heijst, H. J. & Woodhouse, J. H. Complex shear wave velocity structure imaged beneath Africa and Iceland. *Science* **286**, 1925–1928 (1999).

31. Evans, M., Kendall, J.-M. & Willemann, R. Automated SKS splitting and upper-mantle anisotropy beneath Canadian seismic stations. *Geophys J Int* **165**, 931–942 (2006).

32. Wuestefeld, A., Bokelmann, G., Barruol, G. & Montagner, J.-P. Identifying global seismic anisotropy patterns by correlating shear-wave splitting and surface-wave data. *Phys. Earth Planet. Inter.* **176**, 198–212 (2009).

Supplementary Information accompanies the paper on www.nature.com/nature.

Acknowledgements We thank J. Brodholt and D. Dobson for comments. A.N. was supported by NERC. Seismic data were provided by I. Bastow, D. Thompson, and the IRIS and CNSN data centres.

Author contributions *A.N. analysed the data and produced the manuscript and figures. J.W. wrote the analysis and modelling code and performed the modelling. J.W. and J.-M.K. supervised the analysis and commented on the manuscript and figures. All authors discussed the results and implications at all stages.*

Author information Reprints and permissions information are available at www.nature.com/reprints. Correspondence and requests for materials should be addressed to A.N. (email: andy.nowacki@bristol.ac.uk)

Figure 1: Source–receiver geometry, and explanation of φ'. a, Earth section with ray paths for S, ScS and SKS phases. The stippled UM and grey D″ are anisotropic. S turns above D″; ScS samples it. **b,** Data used in this study: seismic stations (triangles); earthquake epicentres (yellow circles); ray paths (thin black lines); ray paths in a 250 km-thick D″ (blue lines); measured source-side shear-wave splitting parameters for shallow earthquakes (black bars beneath circles: length corresponds to delay time, orientation represents fast direction; largest delay time is 2.4 s). We note that fast orientations of shear-wave splitting in the UM beneath shallow earthquakes on plate boundaries are either generally very closely parallel to the plate-spreading direction (EPR and MAR), or to the subduction zone trench (Central America). **c,** Relation of the measured fast directions in the geographic (φ) and ray (φ') reference frames. Because the ScS phase is nearly horizontal for most of its travel through D″, we define $\varphi' = backazimuth - \varphi$, which corresponds to the polarisation away from the vertical of the fast shear wave. In terms of TI, $\varphi' = \pm 90^\circ$ is compatible with VTI, and $-90^\circ < \varphi' < 90^\circ$ implies TTI. This can also be thought of as the plane normal to the rotational symmetry axis being tilted from the horizontal, or dipping, at $(90-\varphi')^\circ$.

Figure 2: Multi-azimuth stacked shear wave splitting results in each region. Also shown are individual D″ ray paths of ScS phases used in stacks (thin grey lines); representative mean ray paths in D″ of stacked measurements (thick black lines, arrows indicate direction of travel); plots of splitting

parameters for each stack at the start of the path (white circles with black bars, angle indicates φ', length indicates δt). Beneath is the variation of V_S at 2750 km depth (~150 km above CMB) in the S20RTS model[30]. Thick red line is cross-section shown in Fig. 3a. Shaded region shows approximate strike of Farallon plate predicted at 2500 km [6]. Three study regions ('W', 'S' and 'E') are indicated by circled areas. Supplementary Fig. 2 shows the approximate finite-frequency zone of sensitivity for ScS in D″.

Figure 3: Section through study region and compatible shear planes for candidate ppv slip systems. a, Cross-section through V_S model S20RTS traversing the study region, as indicated in Fig. 2. The approximate regions W, S and E in D″ are drawn. Colours indicate V_S as for Fig. 2. The inferred location of the Farallon slab from high V_S is labelled with 'FS'. **b–j,** Orientations of potential elastic models which are compatible with the observed anisotropy in D″. Shown are upper hemisphere equal-area projections looking down the Earth radial direction (vertical) of the possible shear planes (coloured lines) and slip directions (black circles) in ppv for each slip system. The colour of the shear planes indicates the amount of strain required to produce them according to the arbitrary colour scale, right. The three slip mechanisms [$\bar{1}$ 10](110) (**b–d**), [100](010) (**e–g**) and [100](001) (**h–i**) are tested in each region (left to right, W, S, E). Up is north. There are usually two sets of planes, because two azimuths of measurements are not sufficient to uniquely define the planes in the orthorhombic symmetry of the models.

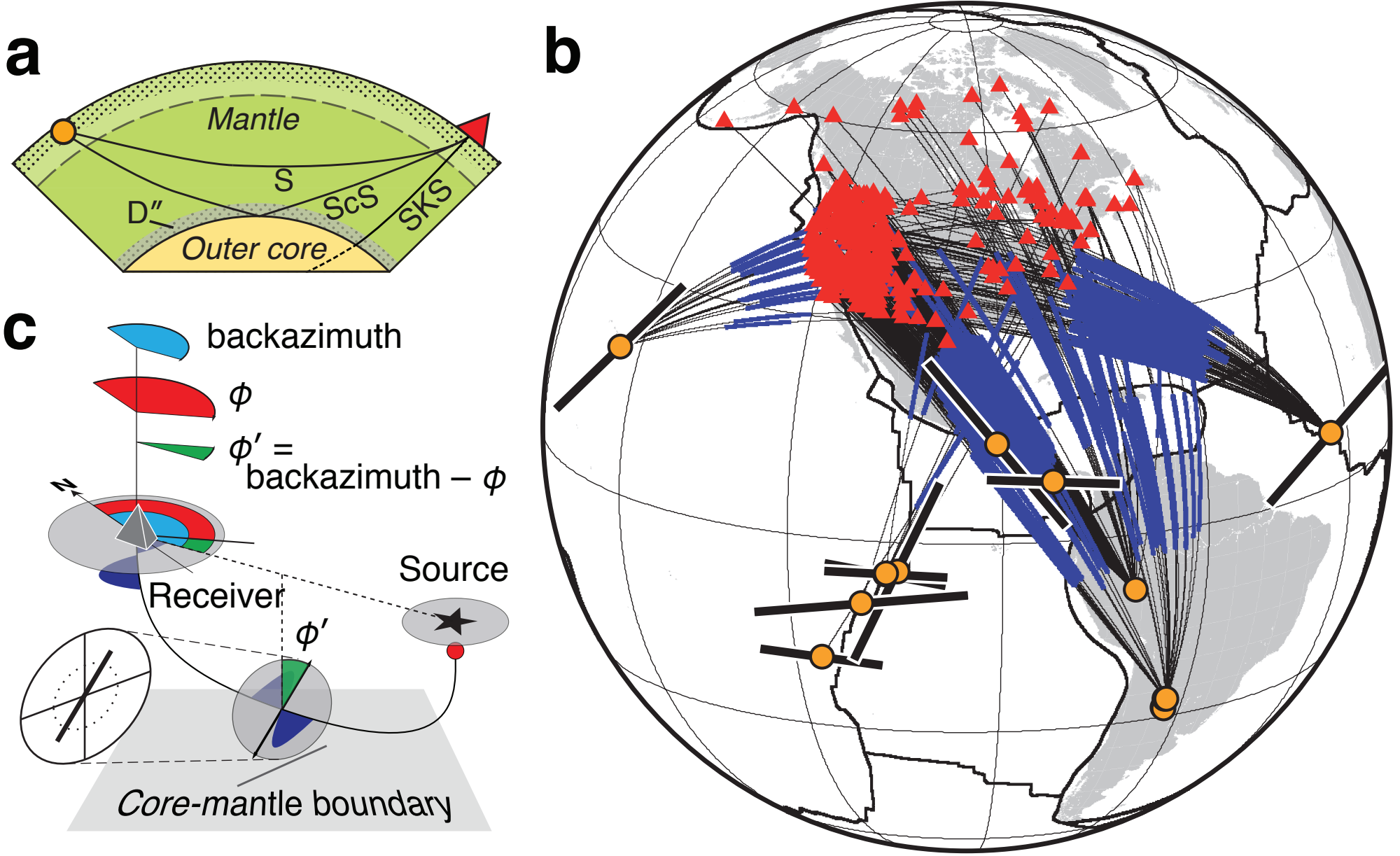
a
Mantle
S
ScS
SKS
D″
Outer core
b
c
backazimuth
ϕ
ϕ′ =
backazimuth – ϕ
N
Source
Receiver
ϕ′
Core-mantle boundary

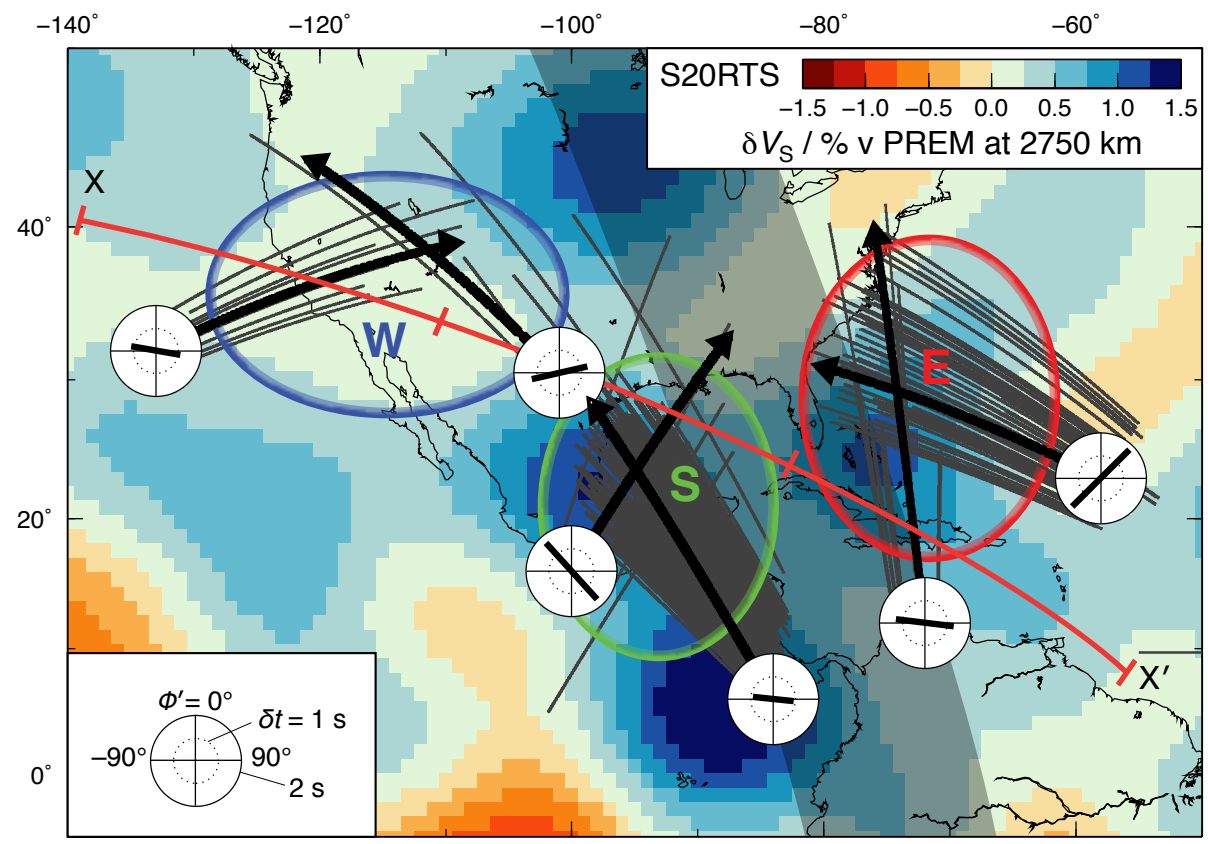
−140°
−120°
−100°
−80°
−60°
40°
20°
0°
S20RTS
−1.5 −1.0 −0.5 0.0 0.5 1.0 1.5
δV_S / % v PREM at 2750 km
X
X′
W
S
E
Φ′ = 0°
δt = 1 s
−90°
90°
2 s

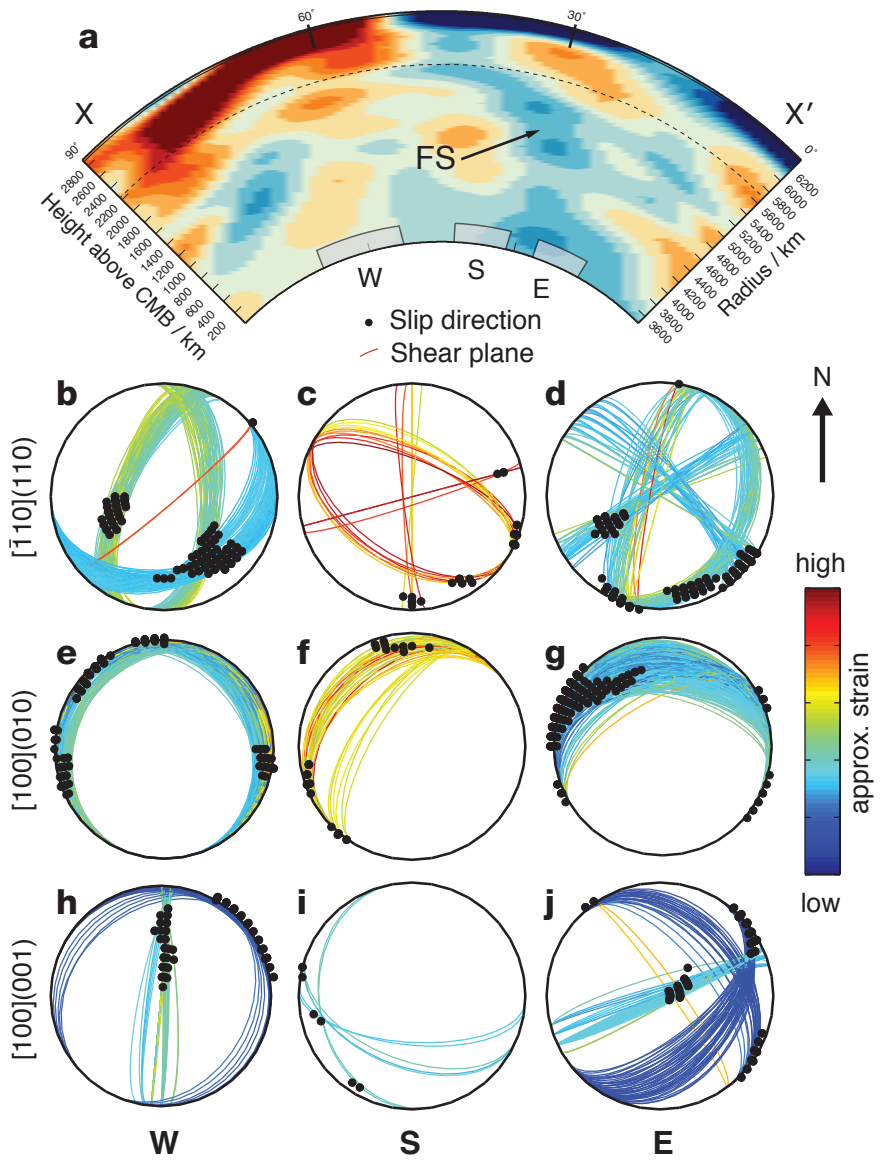
a
60°
30°
X
X′
FS
90°
0°
Height above CMB / km
2800
2600
2400
2200
2000
1800
1600
1400
1200
1000
800
600
400
200
Radius / km
6200
6000
5800
5600
5400
5200
5000
4800
4600
4400
4200
4000
3800
3600
W
S
E
Slip direction
Shear plane
b
c
d
e
f
g
h
i
j
[1̄10](110)
[100](010)
[100](001)
N
high
approx. strain
low
W
S
E

Methods

S–ScS differential splitting We measured differential shear wave splitting between S and ScS phases recorded at ~500 seismic stations in North and Central America, according to the method of ref. [10]. Events of $M_W \geq 5.7$ in the distance range 55–82° were used (Supplementary Table 3), as the two phases then traverse very similar regions of the upper mantle. All data were bandpass filtered between 0.001 and 0.3 Hz to remove noise. We analysed splitting in the phases using the minimum eigenvalue technique[33], with 100 analysis windows in each case to estimate the uncertainties in φ and δt using a statistical F-test[34,35]. An example is shown in Supplementary Fig. 3. The λ_2 surfaces for measurements along each azimuth are stacked[34] in three regions (Fig. 2) to greatly reduce the errors.

Correcting for upper mantle anisotropy We correct for upper mantle (UM) anisotropy using previously published[31,32] SKS splitting measurements (distance >90°) at stations which show little variation of splitting parameters with backazimuth, corresponding to simple UM anisotropy, and where there are measurements made along similar backazimuths to the phases we measure in this study (S, ScS). These provide an estimate of the receiver-side anisotropy, and should eliminate the chance that lateral heterogeneity, or dipping or multiple layers of anisotropy beneath the receiver affect our results. Analysing the splitting in S after applying a receiver-side correction gives an estimate of the source-side splitting beneath the earthquake (Fig. 1b; Supplementary Table 3). For nearby stations with no available SKS measurements, measuring splitting in S whilst correcting for the source anisotropy gives a receiver-side estimate. Both corrections are then applied (for shallow earthquakes; only a receiver-side correction is applied for very deep events >550 km, assuming mantle isotropy below this depth) when analysing ScS, so that the remnant splitting occurs in ScS only, and hence results

from anisotropy in D″ alone. An example of a measurement where both source and receiver corrections are applied is shown in Supplementary Fig. 4.

Testing SKS splitting measurements as upper mantle anisotropy corrections

We test the validity of using SKS measurements as a correction for UM anisotropy. Because the tectonic and geological processes which cause UM anisotropy are unlikely to be determined by structure in D″, we can regard the two as independent. Hence over broad, continental scales, SKS measurements will be oriented approximately randomly, and we can check that the consistency observed in our results is not due to a systematic error being introduced by UM anisotropy. For the MAR event of 2008-144-1935, we analyse the S phase at each station for which we selected reliable SKS measurements, and replace those with others taken at random. The false 'corrections' are determined by allowing the correction fast orientation φ_{corr} to vary between 0 and 180°, and the delay time δt_{corr} between the minimum and maximum values for those in SKS measurements used in this study (0–2.5 s). A uniform random distribution is used. Supplementary Fig. 8 shows polar histograms of φ'', the projected fast orientation at the source, for five of the sets of false 'corrections'. Of these, the smallest sample standard deviation $\sigma_{\varphi''}$=47°. Also shown is that for the true SKS splitting parameters used ($\sigma_{\varphi''}$=33°). Red bars indicate measurements of δt>3.5 s, which may correspond to two situations. Firstly, they may be null measurements, which frequently display a minimum λ_2 at the extreme of the permitted δt (here, 4 s). These arise because by chance the 'correction' applied is the same as the total source-side and receiver splitting combined (i.e., $\varphi_{\mathrm{SKS}} \approx \varphi$ and $\delta t_{\mathrm{SKS}} \approx \delta t$), and by removing the 'correction' there is no remnant splitting. Secondly, the large results may happen when the 'correction' is large and near-perpendicular to the source and receiver splitting at the receiver, leading to very large result, which is extremely unlikely to exist in nature.

It appears that the source side splitting direction (and also delay time; not shown) is most consistent when using SKS measurements to correct for splitting introduced after that beneath the source in S. In addition, φ'' is most similar to the plate spreading direction for the SKS-corrected case.

To confirm that applying an SKS measurement as an UM splitting correction is valid, we check that particle motion is linearised and a null (or very small) measurement results from analysing an S wave from a very deep event. This confirms that the S and SKS waves undergo the same splitting whilst travelling in the UM beneath the station, and hence that the SKS correction is valid. For the event 2007-202-1327, Supplementary Fig. 5 shows the splitting in S at station KAPO with no correction applied and with the SKS measurement of ref. [36] used as a receiver correction (φ_{SKS}=69°, δt_{SKS}=0.58 s). As is evident, with no correction we measure splitting in S to be the same as that in SKS within error. The removal of the splitting leads to a null result, with the particle motion highly linear (Supplementary Fig. 5d).

Source-side anisotropy estimates A further test of the efficacy of correcting for UM anisotropy with SKS measurements, after running the analyses, is to compare the source-side UM splitting that remains after analysing S waves from shallow earthquakes to local splitting measurements. If there is no contamination from unexpected or complicated anisotropy beneath the receiver for which we have not accounted, or for which SKS measurements are not an adequate correction, then source splitting parameters and local ones should be the same. For events at the East Pacific Rise (EPR), we may directly compare φ'' with measurements of SKS splitting using ocean bottom seismometers (OBSs)[37]. These are shown with φ'', δt for the event 1994-246-1156 (Supplementary Fig. 6; Supplementary Table 3). Local splitting and that measured beneath the earthquake are extremely alike. This is also very strong confirmation that

the source correction is a true measurement of source-side splitting, and we can thus remove it comprehensively when analysing ScS.

Source polarisation measurements Another test of the efficacy of using SKS measurements to correct for receiver-side anisotropy is to compare: the polarisations of the linearised particle motion after applying a correction for receiver-side UM anisotropy and measuring the source-side splitting in S; and the predicted source polarisations of the S wave according to the Global CMT solution for that event. For deep earthquakes, we measure the splitting in S and compare the linearised particle motion with the predicted source polarisation without applying any UM correction; for shallow events we apply a correction using SKS measurements. We find that in no case do the measured and predicted source polarisations differ by more than 20°, and in most cases they are within 10°. Supplementary Fig. 7 compares the predicted and measured horizontal particle motions for each earthquake used in this study at an example station.

S–ScS splitting from deep versus shallow earthquakes As a final check that we adequately remove source-side anisotropy, we compare the results of differential analysis of S and ScS using the 2007-202 event (shown to have no measurable source anisotropy in Supplementary Fig. 5) with those from five shallow earthquakes located nearby (Supplementary Table 4). Hence the ray paths are very similar, and the same region of D″ is sampled. If there is any systematic error in our attempt to remove the source-side splitting, the results will be significantly different.

From a larger group of 25 events located near to event 2007-202 above 100 km depth from 1989 onwards, five were selected for good signal-to-noise ratios for both S and ScS. Using $\varphi_{corr}=70^\circ$ and $\delta t_{corr}=0.63$ s (average of S and SKS splitting parameters; see Supplementary Fig. 5), the procedure outlined above was conducted to obtain φ' and δt. Those ray paths for measurements in the S region which traverse the most similar region in D″ to those from the shallow events were selected for comparison

(Supplementary Fig. 9a). Supplementary Fig. 9c–d shows polar histograms of the fast direction in the ray frame, φ', for the two sets of results, with the near-null results downweighted in the shallow case, as the number of data points is small. Because there are few measurements, there is some spread and the standard deviation is relatively large (both of which is reduced when using larger samples; see for instance Supplementary Fig. 11, eastmost histogram). However for the deep event, $\langle\varphi'\rangle \approx 81^\circ$, $\langle\delta t\rangle \approx 1.3$ s; for the shallow events, $\langle\varphi'\rangle \approx -84^\circ$, $\langle\delta t\rangle \approx 1.8$ s. Whilst these are not identical, they are the same within error. The small variation might be due to local variation within D″, as the ray paths do not overlap completely. Where they do, as shown in Supplementary Fig. 9e–f, the results are the same within the 95% confidence limit, further suggesting that the difference between the two groups is mainly small local variation, not a bias in the shallow or deep source region.

This, and the other tests of the use of source and receiver corrections, compels us to believe that the shear wave splitting we observe in ScS after removing UM anisotropy must be the true signal from a third, intermediate anisotropic region—D″.

Mineral slip system fitting To compare different slip systems in ppv, we calculate the orientations of the shear planes and slip directions which are compatible with our measurements. These orientations are computed by performing a grid search over the elastic constants for the relevant slip systems[16,20,25], which are rotated about the three principal (orthogonal) axes; we scale the elastic constants by linearly mixing the fully anisotropic constants with those of an isotropic average. The amount and orientation of shear wave splitting is computed at each node using the Christoffel equation, and orientations which are compatible with the measured anisotropy (within the errors of the azimuthal stacks; Supplementary Table 4) are plotted. The larger the scaling required to fit the case, the higher degree of ‘strain’ is represented (indicated by colour; Fig. 3b–i), and this directly corresponds to the proportion of the material which

is a linear mix of the anisotropic and isotropic components (i.e., the relative proportions of oriented and random crystals).

33. Silver, P. & Chan, W. W. Shear-wave splitting and subcontinental mantle deformation. *J Geophys Res-Sol Ea* **96**, 16429–16454 (1991).

34. Wolfe, C. & Silver, P. Seismic anisotropy of oceanic upper mantle: Shear wave splitting methodologies and observations. *J Geophys Res-Sol Ea* **103**, 749–771 (1998).

35. Teanby, N., Kendall, J. M. & der Baan, M. V. Automation of shear-wave splitting measurements using cluster analysis. *B Seismol Soc Am* **94**, 453–463 (2004).

36. Frederiksen, A. W. *et al.* Lithospheric variations across the Superior Province, Ontario, Canada: Evidence from tomography and shear wave splitting. *J Geophys Res-Sol Ea* **112**, B07318 (2007).

37. Wolfe, C. & Solomon, S. Shear-wave splitting and implications for mantle flow beneath the MELT region of the East Pacific Rise. *Science* **280**, 1230–1232 (1998).